Direct observation of multiband charge density waves in NbTe₂

Won-Jun Jang,[1,*] Junyoung Sim [®],[2,*] Jin Eun Heo,[2] Heeyoon Noh [®],[3] Ryung Kim [®],[2] Seo Hyoung Chang,[2]
Sangjun Jeon [®],[2,†] and Hyo Won Kim[1,‡]

[1]*Samsung Advanced Institute of Technology, Suwon 13595, Republic of Korea*
[2]*Department of Physics, Chung-Ang University, Seoul 06974, Republic of Korea*
[3]*Department of Physics, Yonsei University, Seoul 120-749, Republic of Korea*

The electronic structure of periodic lattice distortion (PLD) in NbTe₂ was examined using low-temperature scanning tunneling spectroscopy and microscopy. The striped PLDs with 3×1 and $1 \times \frac{9}{2}$ superstructures were characterized in real and reciprocal space. The simultaneous formation of momentum-specific suppressions in the spectral weight and phase shifts of the wavefront related to the superstructures were observed at multiple energies. These unusual energy dependencies are well agreed with the charge density waves (CDWs) formed in the multiband electronic structure of NbTe₂. Fermi-surface nesting and reconstruction of the reciprocal lattice were suggested in developing the multiband CDWs in NbTe₂.

I. INTRODUCTION

The electronic states of low-dimensional materials are susceptible to electron-electron and electron-phonon interactions [1,2]. These many-body interactions often result in charge density waves (CDWs) in layered systems with considerably modified Fermi-surface symmetry and shape [3–6]. The Peierls model explains the essence of CDW formation in a one-dimensional (1D) system owing to electron-lattice instability. The total energy of the system decreases because of spontaneous periodic modulation of the atomic lattice with a well-defined wave vector [3,7]. Fermi-surface nesting is a generalization of the Peierls model that is used to describe a CDW in higher dimensions. The formation mechanism involves lattice instability induced by a phonon mode that connects the nested Fermi surface. As a result, it is predicted that an abnormal electronic susceptibility and Kohn anomaly occur at the same momentum, and a metal-insulator transition is expected below the phase transition temperature (T_{CDW}) [3,8–10]. However, the partial absence of the expected experimental signatures in CDWs requires a model beyond simple Fermi-surface nesting. The strong electron-phonon interaction [8,9,11] and, more recently, multiband CDW formation, has been suggested as an alternative explanation for unusual CDWs [12].

NbTe₂ belongs to a family of layered transition metal dichalcogenides (TMDCs) that simultaneously exhibits strong periodic lattice distortion (PLD) and superconductivity. Previous studies using low-energy electron diffraction observed a 3×1 superstructure from multiple domains [13,14], scanning tunneling microscopy (STM) visualized 1D atomic rows of tellurium atoms [15], and a neutron experiment reported a $\sqrt{19} \times \sqrt{19}$ CDW under heat pulse treatment [14]. However, the origin of stabilizing the observed PLDs has not been establised. The Fermi-surface nesting and electron-phonon coupling were proposed to be crucial in lowering the crystal symmetry [13]. Still, the detailed properties of these mechanisms have not yet been fully characterized. The experimental signature of structural phase transition and the predicted density of states (DOS) gap at the Fermi level has not been observed [16–18]. The formation of multiband CDWs and their geometrical relationships have also not yet been discussed. Moreover, recent interest in the topological character of NbTe₂ has increased the importance of CDWs in this material. A theoretical study using symmetry indicators classified NbTe₂ as a topological semimetal [19], and a low-temperature study reported unconventional superconductivity as possibly inherited from the nontrivial topology of the band [20]. Therefore, comprehensive microscopic studies are required to identify the modified electronic states of NbTe₂.

In this paper, we report two striped patterned PLDs with orthogonal directions on the surface of NbTe₂. One PLD was 3×1 commensurate with the lattice, whereas another PLD was quasiperiodic. In contrast to previous results, we found that the second PLD had a locally commensurate $1 \times \frac{9}{2}$ order with continuous phase slip rather than a triple axis ($\sqrt{19} \times \sqrt{19}$) or single axis ($\sqrt{19} \times 3\sqrt{3}/2$), which were reported previously [14,21,22]. The suppressions of spectral weight were clearly observed at the wave vectors defining the PLDs. The phase shift of spatial modulation was not simply a π shift across the energy of spectral weight suppressions and was highly energy dependent for both PLDs. By analyzing the spectroscopic measurements in real and reciprocal space, we found that the formation of PLDs in NbTe₂ was associated with multiband CDWs along the Γ-M and Γ-K directions. The observation of domain boundaries with $120°$ in angle supports the spontaneous symmetry breaking after a phase transition. These observations were reproduced with a model simulation and well agreed with the previous first-principle calculation

---

*These authors contributed equally to this work.

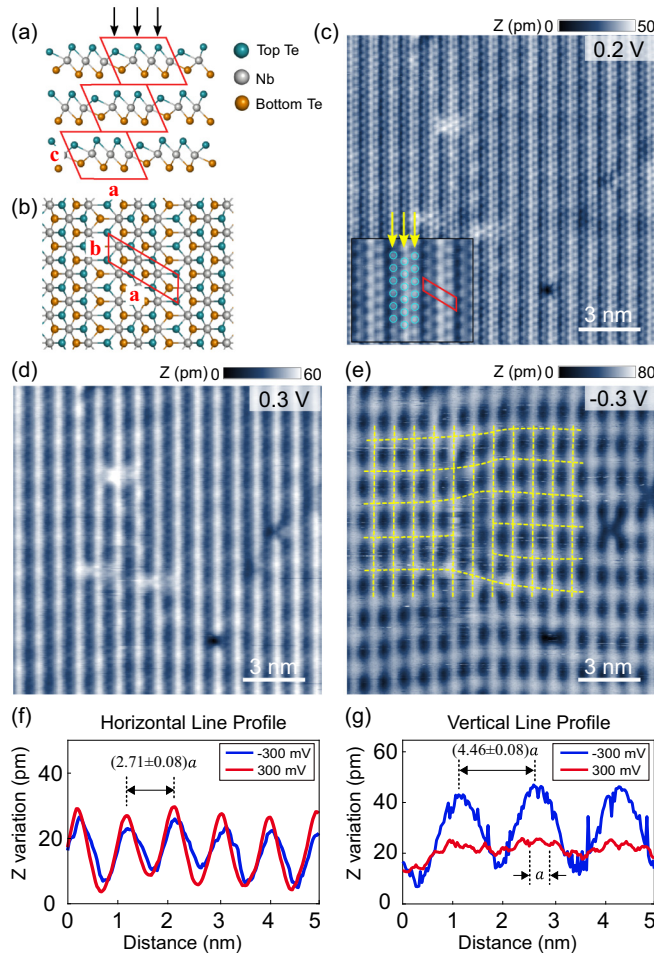†jsangjun@cau.ac.kr

‡hyowon98.kim@samsung.com

FIG. 1. Bulk crystal structure and scanning tunneling microscopy (STM) topographs of NbTe$_2$. (a) Side view and (b) top view of a schematic of the crystal structure of monoclinically distorted NbTe$_2$. The Nb atoms (gray) are sandwiched between the top (cyan) and bottom (orange) Te atoms within a monoclinic conventional unit cell (red parallelograms). (c) Topographic STM image of the NbTe$_2$ surface ($V = 200$ mV, $I = 100$ pA). Striped patterns along the vertical direction of the image correspond to the 3×1 superstructure (monoclinic distortion). Inset shows a closeup image of the surface displaying the position of the top Te atoms (cyan circles). The yellow arrows indicate the position of the three Te atoms specified in (a). The red parallelogram shows the monoclinic unit cell presented in (b). (d), (e) Topographic STM images ($I = 100$ pA) measured with a bias of (d) $V = 300$ mV and (e) $V = -300$ mV. The dashed yellow lines in (e) indicate the dislocation of the PLDs. The data in (c)–(e) were measured in the same region. (f), (g) Line profiles of the height variation measured with $V = 300$ and -300 mV, taken along horizontal and vertical line in (d) and (e).

[13]. Therefore, Fermi-surface nesting and reconstruction of the reciprocal lattice by a strong electron-phonon coupling is important in understanding the electronic structure of NbTe$_2$.

II. CRYSTAL STRUCTURE AND ATOMIC DISTORTION

We first identified the crystal structure of NbTe$_2$ by performing x-ray diffraction (XRD) at room temperature. The XRD results showed that NbTe$_2$ had a mixed structure in
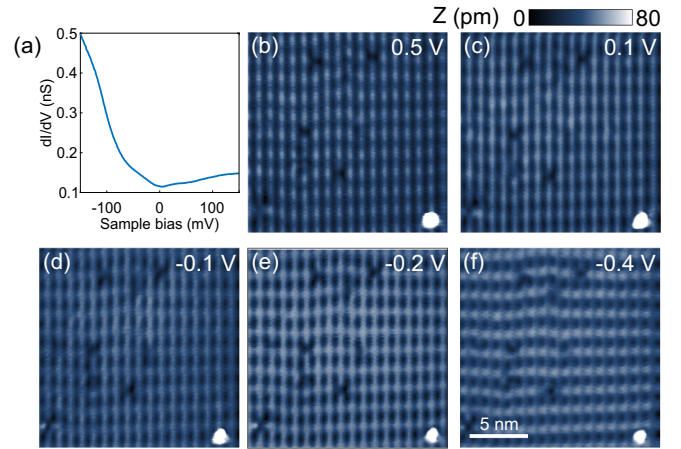

FIG. 2. (a) A spatially averaged dI/dV curve of NbTe$_2$. (b)–(f) Topographic STM image ($I = 200$ pA) with detailed energy dependence. The topographic data were acquired in the same region.

which the trigonal and monoclinic phases coexisted. This bulk crystal structure was in good agreement with a report that NbTe$_2$ is in a monoclinically deformed trigonal phase with a $3 \times 1 \times 3$ structure [13,15,17,18,23]. The formation of domains from the striped PLDs resulted in abnormal peaks in the XRD measurements (see Appendix A). The deformation existed at room temperature, and no additional structural phase transition was reported below room temperature until the superconducting transition at 0.75 K [17,20,24].

A schematic of the crystal structure of unidirectionally distorted NbTe$_2$ within a single domain is shown in Fig. 1(a). Three Nb atoms sandwiched by six Te atoms formed a unit cell of the monoclinic phase [red parallelogram in Figs. 1(a) and 1(b)] with a 3×1 superstructure was constructed on the *ab* plane. Figure 1(c) shows a typical STM topography of cleaved NbTe$_2$ with atomic resolution. All STM measurements were performed at the temperature of 2.7 K. The cleavage plane observed in our STM studies was located at the center of the Te layers because of weak van der Waals interactions between the layers. The position of the surface Te atoms was deformed from the trigonal lattice and formed a well-ordered striped pattern composed of three Te atoms. The yellow arrows in the inset of Fig. 1(c) indicate the three Te atoms with different topographic heights corresponding to the top three Te atoms in the unit cell, as depicted in Fig. 1(a). By analyzing the period and direction of the measured pattern, the vertical striped pattern was identified as a 3×1 PLD, which was perfectly commensurate with the crystal lattice. The amplitude of the charge modulation measured from the topographic height changed as we varied the bias voltage applied to the sample, as shown in Figs. 1(d) and 1(f). The wavelength is measured to be 2.71 ± 0.08 times the undistorted atomic spacing.

We found additional charge modulation orthogonal to the 3×1 PLDs in the STM image measured with an applied bias voltage of -300 mV, as shown in Fig. 1(e). In contrast to the 3×1 commensurate PLD, the wavefront of the horizontal striped pattern was not locked with the lattice, as indicated by the existence of dislocation in Fig. 1(e). The subsurface impurities imaged as white protrusions modified the
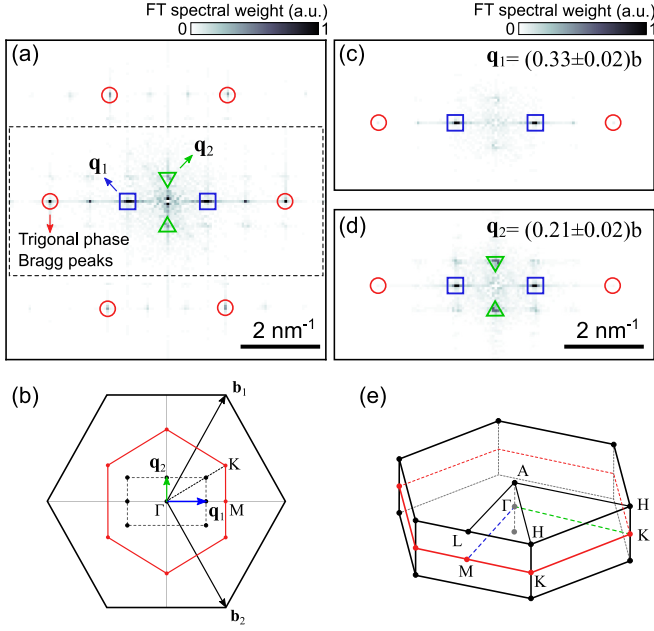
FIG. 3. Fourier analysis of lattice modulations. (a) Fast Fourier transform (FFT) map of Fig. 1(c). Peaks indicated by red circles represent periodicity from trigonally arranged Te atoms. The blue squares and green triangles correspond to the vertical (q_1) and horizontal (q_2) striped patterns in Fig. 1(c), respectively. (b) Schematic diagram of the reciprocal lattice of the NbTe$_2$ surface. Corners of the black hexagon are reciprocal lattice points corresponding to Bragg peaks in (a). The red hexagon represents the first Brillouin zone constructed from the black hexagon. (c), (d) FFT map of Figs. 1(d) and 1(e), respectively. The plot range is the same as the dashed black rectangle in (a). The peak intensities of q_1 and q_2 are comparable in (d), whereas the intensities are distinct in (c). (e) Schematic diagram of the three-dimensional Brillouin zone of undistorted NbTe$_2$. The wave vector q_2 is parallel to Γ-K and A-H.

periodicity of the horizontal PLD, whereas the surface Te vacancies [black dots in Fig. 1(c)] did not affect PLD formation. This topographic observation indicated the weak interlayer coupling of the horizontal PLD compared to the relatively strong interlayer connection for the commensurate 3×1 PLD, which showed robust lattice deformation against imperfections. The local periodicity of the horizontal PLD on a defect-free region was 4.46 ± 0.08 times the atomic spacing, and the modulation amplitude was also highly energy dependent, as displayed in Figs. 1(g) and 2.

III. FOURIER ANALYSIS OF LATTICE MODULATIONS

A two-dimensional fast Fourier transform (FFT) analysis further clarified the momentum characteristics of the two PLDs. Figure 3(a) shows the FFT map of Fig. 1(c). The hexagonal Bragg peaks from the trigonally arranged Te atoms are marked by red circles. Wave vector q_1 (blue rectangles) corresponded to the periodicity of the 3×1 superstructure located at $\frac{1}{3}$ of the wave vector pointing to a Bragg peak, $|q_1| = b/3$, where b is the length of the reciprocal vectors [Figs. 3(b) and 3(c)]. Wave vector q_2 (green triangles) was relevant to the horizontal striped pattern points in the Γ-K direction and perpendicular to the q_1 vector. The length of the q_2 vector
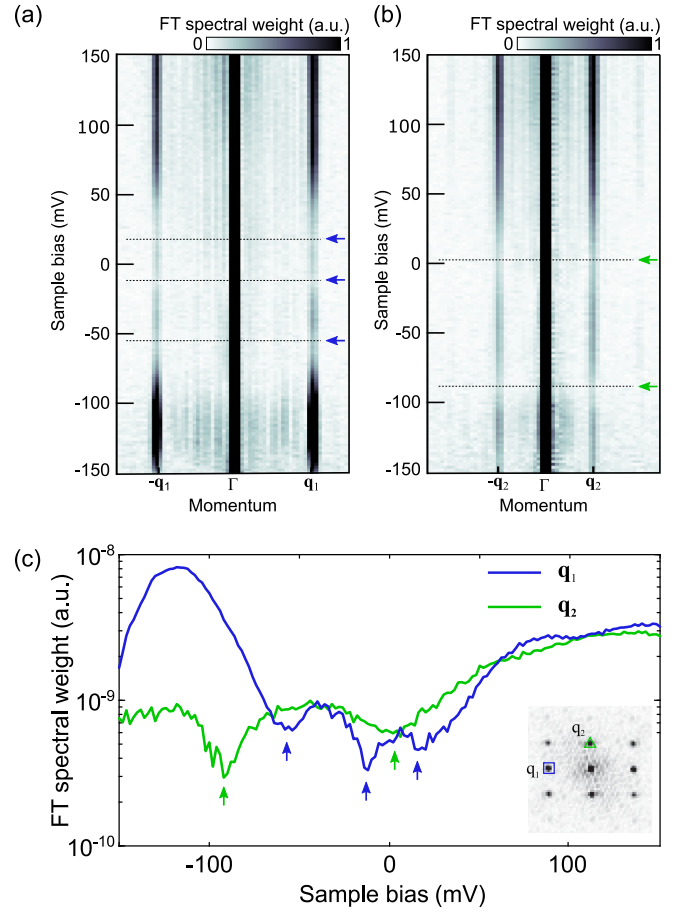

FIG. 4. Energy-dependent intensity variation of PLD spectral weight. (a), (b) Plots of Fourier transform (FT) spectral weight from the $dI/dV(r, V)$ spectroscopic map ($V_{set} = -150$ mV, $I_{set} = 150$ pA, $V_{mod} = 10$ mV) cut along the momentum (a) $-q_1$–Γ–q_1 and (b) $-q_2$–Γ–q_2. The peaks of q_1 and q_2 are nondispersive but have an energy dependency in their intensity. (c) A semilogarithm plot of FT peak spectra at q_1 and q_2. The blue and green arrows indicate the energy of intensity suppression. The values of energy and width of the spectral weight suppressions are summarized in Table I of Appendix B. Inset shows the Fourier-transformed scanning tunneling spectroscopy map at 150 mV to mark the peak positions where each spectral weight is taken.

is measured to be 0.21 ± 0.02 times the reciprocal lattice constant b and approximately $\frac{b}{3\sqrt{3}}$ within the resolution of our FFT analysis. All the unmarked peak positions in Figs. 3(a), 3(c), and 3(d) can be obtained as integer combinations of the wave vectors of q_1, q_2, and the Bragg peaks.

The positions of the q_1 and q_2 wave vectors with different measurement biases remained at the same points in the reciprocal space, as shown in Figs. 3(c) and 3(d). However, the intensity of the peaks representing the strength of lattice modulation varied with energy. This modification of the DOS due to the PLDs was further analyzed by constructing FFT maps from energy-resolved scanning tunneling spectroscopy (STS) maps. Figures 4(a) and 4(b) display the FT spectral weight as a function of voltage following the direction of the q_1 and q_2 wave vectors, respectively. The wave vectors q_1 and q_2 were energetically nondispersive and persisted across

TABLE I. Parameters used in the CDW simulation.

CDW		ε_i (meV)	Δ_i (meV)	ϕ_i (°)[a]	λ_i (nm)
$\mathbf{q}_1$	ρ_1[b]	-160	20	0	0.955
	ρ_2[c]	-57.4	8.9	120	0.955
	ρ_3[c]	-12.8	5.4	0	0.955
	ρ_4[c]	17.9	2.3	120	0.955
	ρ_5[b]	160	20	240	0.955
$\mathbf{q}_2$	ρ_1[b]	-200	20	120	1.57
	ρ_2[c]	-91.6	15.3	0	1.57
	ρ_3[c]	0.95	24.2	120	1.57
	ρ_4[b]	200	20	0	1.57

[a]The phase difference values were selected to reproduce the experimental data.
[b]Added to reproduce the experimental data.
[c]Extracted CDW parameters from the experimental data.

a wide energy range. The intensity of $\mathbf{q}_1$ exhibited multiple suppressions near the Fermi energy, as indicated by the blue arrows in Figs. 4(a) and 4(c). The intensity corresponding

to the $\mathbf{q}_2$ peak exhibited mild suppression near the Fermi energy and additional suppression at -92 mV, as indicated by the green arrows in Figs. 4(b) and 4(c). The position and width of the suppressions are summarized in Table I. Note that while the spatially averaged dI/dV spectra did not show a gaplike feature around neither the Fermi energy nor -92 mV [Fig. 2(a)], the FFT analysis clearly exhibited hidden momentum-specific DOS suppressions related to the PLDs.

IV. DISCUSSION

To clarify the mechanism of PLD formation in NbTe$_2$, we compared our FFT analysis results with previous *ab initio* calculations [13]. The susceptibility calculation for NbTe$_2$ with trigonal symmetry showed a strong nesting vector along the Γ-M direction, matching the 3×1 superstructure specified by the $\mathbf{q}_1$ vector. With the imaginary phonon mode at the center of the Γ-M direction, the dominant mechanism in developing the $\mathbf{q}_1$ modulation was strongly supported by CDW formation from the Fermi-surface nesting mechanism. The susceptibility calculation also revealed secondary peaks at $|\mathbf{q}| = 0.19b$
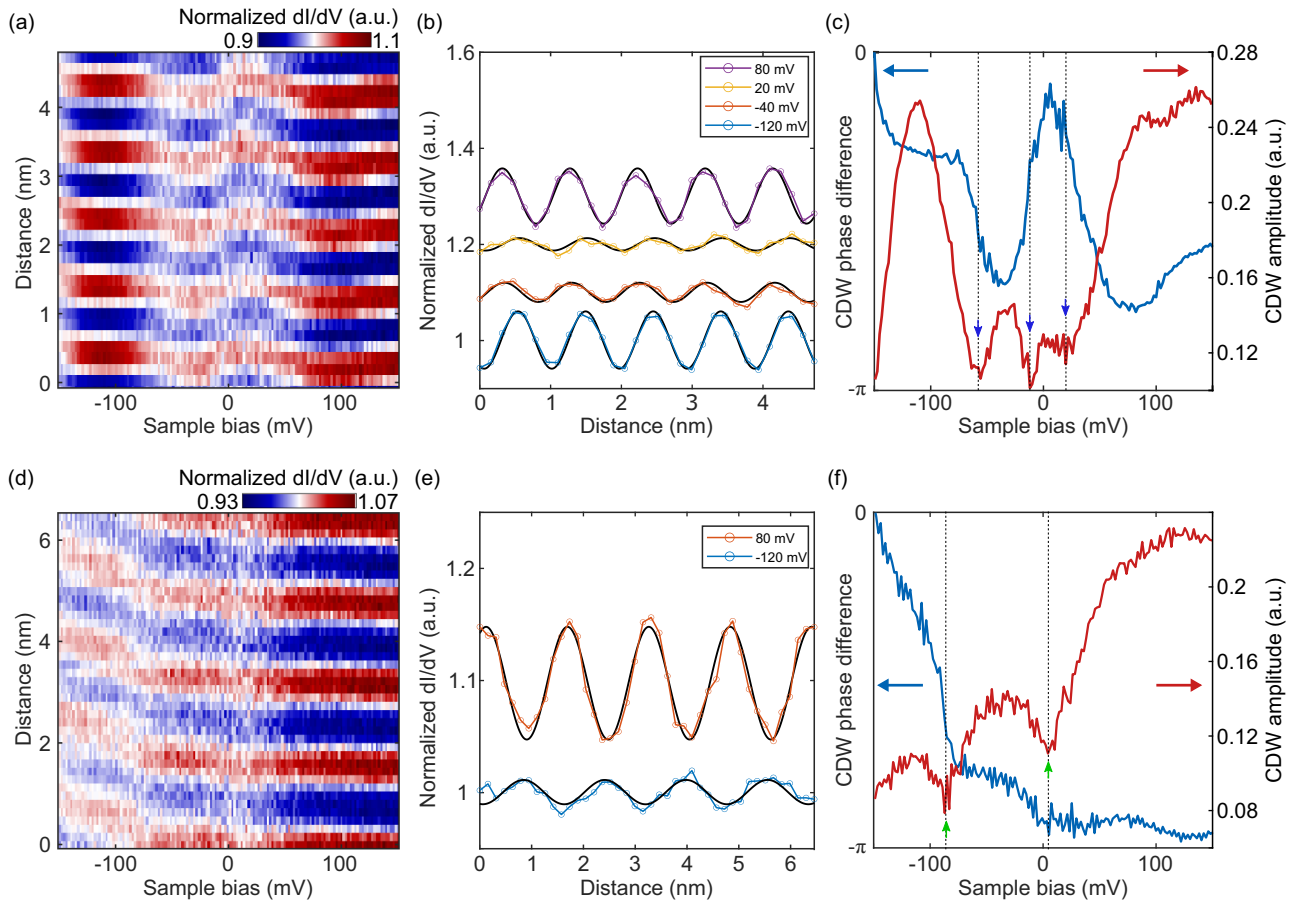

FIG. 5. Energy-dependent amplitude and phase of periodic lattice distortion (PLD). (a) Spatially averaged $dI/dV(r, V)$ map. The image is constructed from the scanning tunneling spectroscopy maps acquired at an impurity-free region and spatially averaged along the axis perpendicular to the $\mathbf{q}_1$ vector for every measurement bias. The $dI/dV(r, V)$ data were further normalized by the spatially averaged conductance to extract the amplitude and phase variation in energy. (b) Tunneling conductance modulations of the 3×1 superstructure at various energies and their sine fittings (black curves). For the sine fitting, a wavelength of $\lambda = 0.955$ nm is used. (c) Bias dependency of the phase and amplitude of the 3×1 PLD extracted from the sine fitting. (d)–(f) Energy dependency of the amplitude and phase of the $1 \times \frac{9}{2}$ PLD plotted in the same way as (a)–(c). $\lambda = 1.57$ nm is used for the sine fitting.
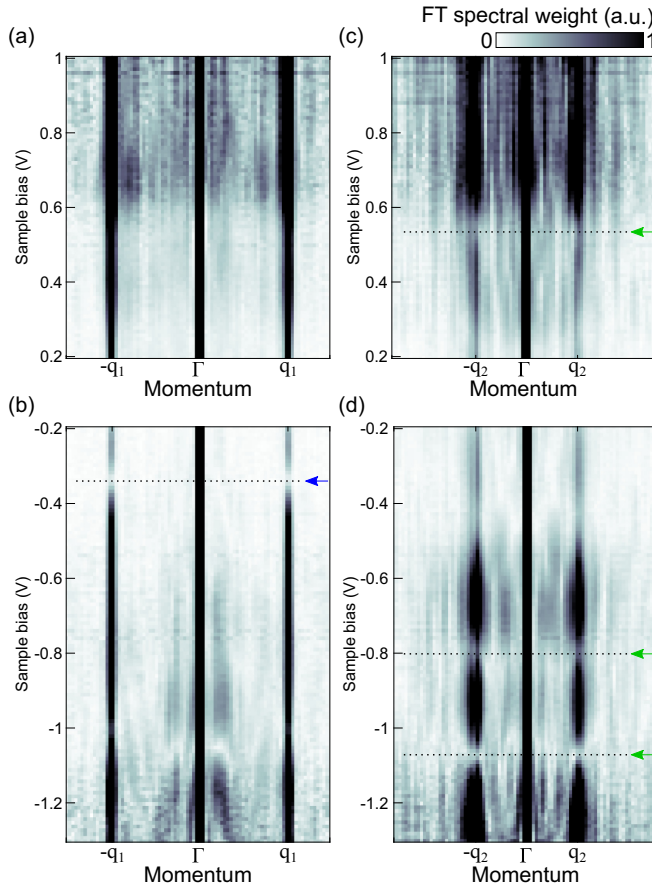
FIG. 6. Plots of FFT spectral weight of $dI/dV(r, V)$ spectroscopic map over a large bias range for momentum cuts (a), (b) $-\mathbf{q}_1–\Gamma–\mathbf{q}_1$ and (c), (d) $-\mathbf{q}_2–\Gamma–\mathbf{q}_2$. The momentum peaks relevant to $\mathbf{q}_1$ and $\mathbf{q}_2$ CDW exist in a wide energy range. The suppressions of CDW amplitude is indicated with arrows at -0.35 V for $\mathbf{q}_1$ CDW and 0.5, -0.8, and -1.1 V for $\mathbf{q}_2$ CDW.

FIG. 7. Topographic STM images at (a) $V = 200$ mV, $I = 50$ pA, and (b) $V = -200$ mV, $I = 50$ pA with domain boundaries at NbTe$_2$ surface. The yellow guide line follows the 3×1 periodic lattice distortion across the boundaries.

along the Γ-K direction, which precisely matched the wave vector $\mathbf{q}_2$ [$= b/(3\sqrt{3}) \sim 0.19b$] that defined the $1 \times \frac{9}{2}$ modulation. The phonon calculation also showed an imaginary phonon mode at the center of the A-H direction, parallel to the Γ-K direction. The length of the phonon mode was analogous to the $\mathbf{q}_2$ vector [see Fig. 3(e) for the bulk Brillouin zone of NbTe$_2$ with trigonal symmetry]. The local periodicity of $\mathbf{q}_2$ vector measured from the real-space map precisely matches the $1 \times \frac{9}{2}$ order. The global periodicity obtained from the FFT analysis is also consistent with the $1 \times \frac{9}{2}$ order within our measurement resolution. Thus, with the experimental data and the first-principle calculation, the lattice distortion relevant to $\mathbf{q}_2$ vector is a $1 \times \frac{9}{2}$ CDW rather than $\sqrt{19} \times \sqrt{19}$ or $\sqrt{19} \times 3\sqrt{3}/2$. The amplitude suppression of the $\mathbf{q}_2$ CDW around the Fermi energy in our FFT analysis suggested that the formation of the $1 \times \frac{9}{2}$ CDW was again consistent with the phonon-mediated Fermi-surface nesting mechanism. The full gap associated with the 2D CDW in the toy model was hindered in our data because the metallic DOS of bulk NbTe$_2$ cannot be ignored in our tunneling spectroscopic measurement. Although the $\mathbf{q}_2$ CDW was not locked with the atomic lattice, it is a commensurate CDW because the local period-
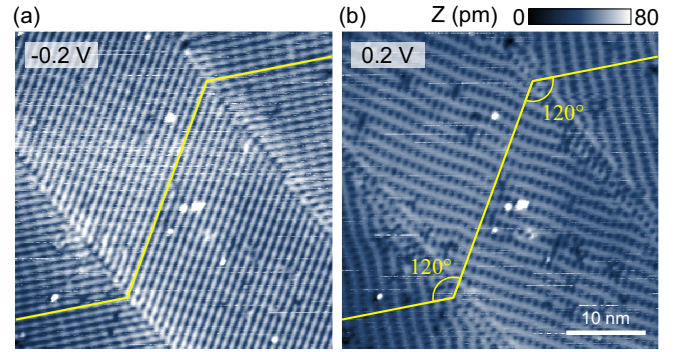
icity is a rational ratio with the atomic lattice constant. The change of periodicity observed in the real space [for example, Fig. 1(e)] can be related to the local phase variation due to a dislocation [25].

However, observing multiple suppressions in the FT spectral weight requires further explanation compared to those in the single-band model. Recently, multiple DOS suppressions and nontrivial phase shifts in topographic modulations have been studied in NbSe$_2$ and TiSe$_2$ [10,12]. The authors demonstrated that CDW formation in a multiband system could produce experimental observations. This argument can be applied to examine multiple DOS suppressions in NbTe$_2$. Figures 5(a) and 5(d) show the energy-dependent amplitude and phase of the 3×1 and $1 \times \frac{9}{2}$ PLD, respectively. The local conductance normalized by the average conductance was used to visualize each modulation's amplitude and phase shift in Fig. 5. The peak positions of charge modulation for each bias were fitted using the sine function $\rho(E, x) = I(E) \sin(\frac{2\pi}{\lambda} x - \phi(E))$, where λ is the wavelength of each modulation. The data and fitted results [black lines in Figs. 5(b) and 5(e)] clearly showed the amplitude $I(E, x)$ and phase $\phi(E)$ variation in energy. The charge modulations changed their phases $\phi(E)$ across the energies at which the amplitudes $I(E)$ were suppressed, as shown in Figs. 5(c) and 5(f). Note that because the spectroscopic measurements were performed with the tip-sample distance stabilized by the set energy (-150 mV in this measurement), the acquired phase shift is a relative phase shift referenced from the phase of set energy and has artificial offset.

The accumulated charge and depleted regions measured by STM are known to have contrast inversion with a bias above and below the CDW gap [10,26,27]. However, this π-phase shift is applicable only to CDWs from a single band. As in the case of NbSe$_2$, the phase shift across a CDW gap can have a complex energy structure if CDWs form in multiple bands [12]. The charge order of each band has the freedom to choose a charge modulation phase in real space, depending on the phase-locking mechanism. To minimize the energy cost from the lattice strain, the relative phase shift between the commensurate CDWs prefers a rational fraction of 2π [28]. From our simulation of the 1D CDW, we reproduced the complex phase variation in our measurements by using the
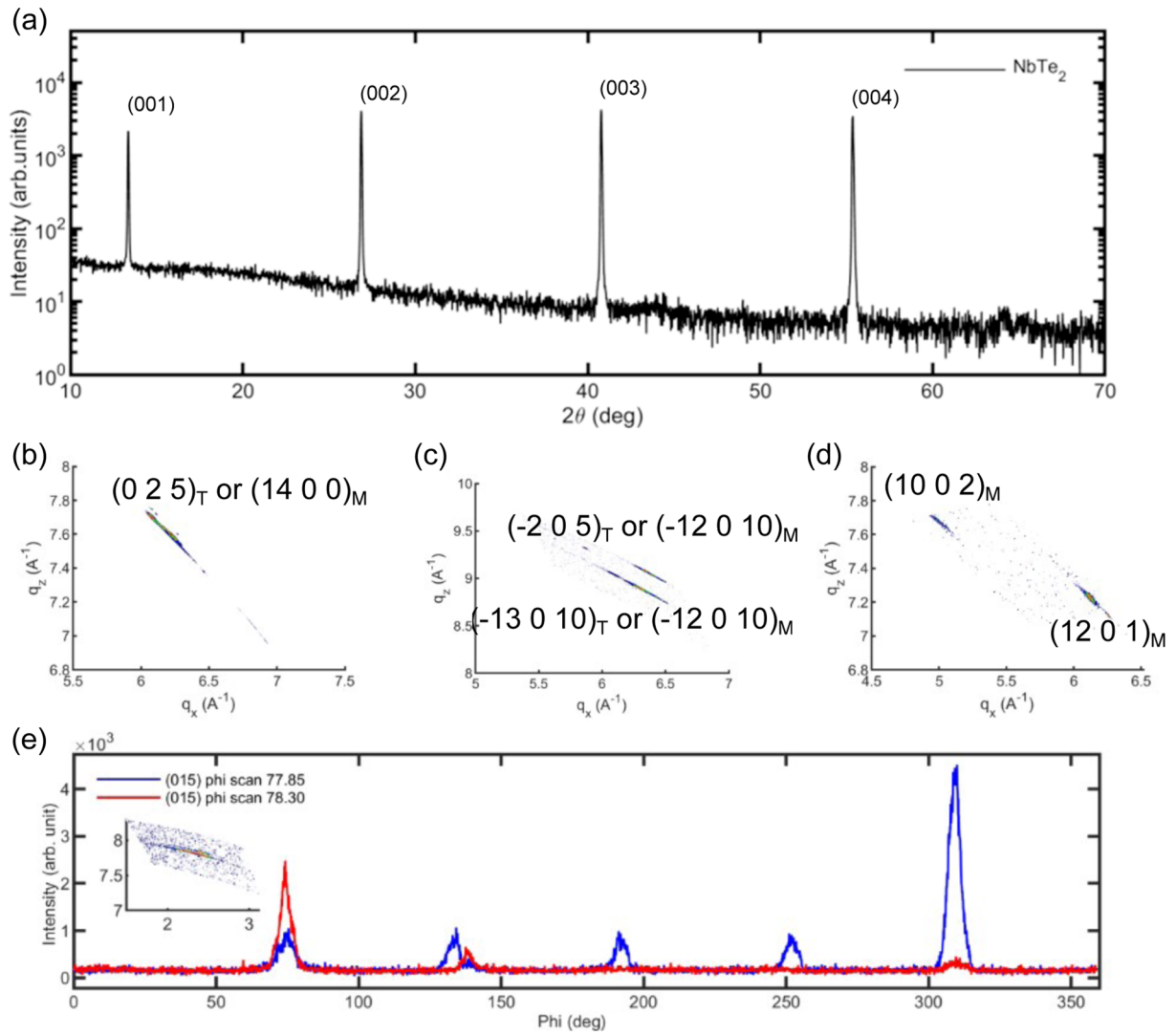
FIG. 8. XRD measurements to identify crystal structure of $NbTe_2$. (a) Off specular scan of $NbTe_2$. $(h\,k\,l)_T$ and $(h\,k\,l)_M$ correspond to a trigonal phase and a monoclinic phase, respectively. (b)–(d) Reciprocal space mapping (RSM) measurement of $NbTe_2$ which aligned at (b) $(0\,2\,5)_T$ or $(14\,0\,0)_M$, (c) $(0\,-2\,6)_T$ or $(-12\,0\,10)_M$ and (d) $(10\,0\,2)_M$ or $(12\,0\,1)_M$. There is no existence of a trigonal phase near $(10\,0\,2)_M$ peak. (e) Phi scan measurement of $(0\,1\,5)_T$ position with two angles $2\theta = 77.85°$ and $78.30°$. Inset shows the RSM at $\phi = 14.43$.

extracted CDW gaps with a phase difference between bands (see Appendix B).

The first-principles calculation of $NbTe_2$ revealed multiple bands dispersed around the Γ point within the energy window of 100 meV [13,17]. Thus far, experimental analyses and theoretical computations on $NbTe_2$ have focused on the topmost band that crosses the Fermi energy following the single-band model. However, other bands can develop a momentum-specific DOS gap away from the Fermi energy. One possibility is that the reconstructed reciprocal lattice from the charge modulations at the Fermi energy [dashed rectangle in Fig. 3(b)] results in additional level repulsions at the wave vector $\mathbf{q}_{CDW}$ far from the Fermi energy. The FFT data with an extended energy range revealed momentum-dependent DOS suppressions far ($\sim$1 eV) from the Fermi energy, as shown in Fig. 6. This spectroscopic observation supports the crucial role of the reshaped band structure in the development of multiple DOS suppressions in $NbTe_2$. Note that the $\mathbf{q}_1$ vector originated from periodic atomic distortion,

similar to the Bragg points from a crystal lattice. The robust presence of the $\mathbf{q}_2$ vector for the entire measured energy range implied a strong electron-phonon interaction because the corresponding $1 \times \frac{9}{2}$ PLD was not locked with with the crystal lattice.

$NbTe_2$ has domains of lattice modulations, as shown in Fig. 7. The angles between domains are multiples of 120°. The spontaneous symmetry breaking from a single crystalline with threefold symmetry is a possible origin of this angle restriction. This observation, together with the characteristics of CDWs, suggests the multiband CDWs stabilize the deformation in $NbTe_2$. Strikingly, even with these various domains, the directions of the $\mathbf{q}_1$ and $\mathbf{q}_2$ vectors maintain an orthogonal relation within the domains. Susceptibility calculations with trigonal symmetry [13] showed that each CDW could take three equally possible wave vectors for $\mathbf{q}_1$ and $\mathbf{q}_2$. However, our measurements showed that the $1 \times \frac{9}{2}$ PLD always took the wave vector $\mathbf{q}_2$ perpendicular to the wave vector of the 3×1 PLD. Although the characteristic behaviors of the two

PLDs/CDWs in NbTe$_2$ were distinct, this geometrical restriction implied that both PLDs were intimately connected in their formation.

V. CONCLUSION

In this low-temperature STM study, we observed 3×1 and $1 \times \frac{9}{2}$ PLDs on the surface of NbTe$_2$ at atomic resolution. We discuss the mechanism of PLD formation by analyzing spectroscopic measurements in real and reciprocal space. Combining the spectroscopic data with previous first-principle calculations, we suggested that PLDs resulted from CDW formation by the Fermi-surface nesting in the trigonal structure of NbTe$_2$. The intensity and phase variation of charge modulation in energy strongly suggested the development of CDW gaps in multiple bands along the Γ-M and Γ-K directions. We also investigated the role of the reciprocal lattice reconstructed by the CDWs to explain DOS suppression deep below the Fermi energy. The modified shape and symmetry of the reciprocal lattice and Fermi surface owing to CDW formation enriched the topology of the NbTe$_2$ bands. The direct CDW measurement and the analysis methods used in this study can be extended to redefine the band topology of TMDC materials.

ACKNOWLEDGMENTS

APPENDIX A: X-RAY DIFFRACTION MEASUREMENTS ON NbTe$_2$

We performed x-ray diffraction (XRD) measurements using a high-resolution x-ray diffractometer (Bruker AXS D8 with a 2D detector and Cu $K\alpha 1$ source) to verify the crystal structure of NbTe$_2$, as shown in Fig. 8. Figure 8(a) exhibited the single-crystal-like structure of NbTe$_2$ crystal with an out-of-plane direction. Reciprocal space mapping (RSM) measurements in Figs. 8(b) and 8(c) showed the nonspecular rod peaks, which can be assigned by both trigonal (denoted by subscript T) and monoclinic (denoted by subscript M) structures. However, the corresponding peaks in Fig. 8(d) were only assigned by the monoclinic structure. To verify the crystal structure of the NbTe$_2$ crystal, we performed the phi scan at $2\theta = 77.85°$ and $78.30°$ for the trigonal structure (0 1 5)$_T$ peak, which is close to the monoclinic structure $(-3 \pm 1\ 6)_M$ or $(3 \pm 1\ 4)_M$ peak, displayed in Fig. 8(e). Intriguingly, we observed multiple peaks with a phi difference of about 60°, which translates to the threefold symmetry of a trigonal phase with different domains rather than a monoclinic structure. Therefore, based on RSM and in-plane structural measurements, NbTe$_2$ crystal can have monoclinic and trigonal phases with different domains.
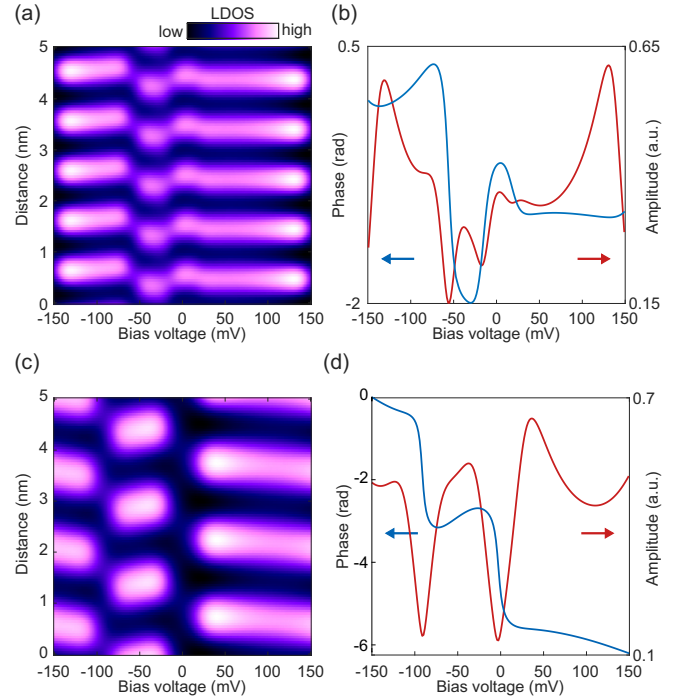

FIG. 9. Simulations of LDOS(E, x) for $\mathbf{q}_1$ and $\mathbf{q}_2$ CDW. (a) Simulation results for $\mathbf{q}_1$ with five CDW gaps. (b) The bias-dependent phase shift and amplitude of CDW modulations of (a). (c) Simulation results for $\mathbf{q}_2$ with three CDW gaps. (d) The bias-dependent phase shift and amplitude of CDW modulations of (c). The parameters used for capturing the experimental features are summarized in Table I. A broadening factor of $\gamma = 15$ mV was used for the simulation.

APPENDIX B: SIMULATION RESULTS OF MULTIBAND CDWs

The unusual phase shifts in the momentum-specific DOS with the $\mathbf{q}_1$ and $\mathbf{q}_2$ PLD were reproduced by a 1D CDW model with multiple gaps. The energy-dependent local DOS of 1D CDW is described by the following equation [12,26,29]:

$$\rho(E, x) = \rho_o \left(1 - \frac{\Delta}{E - \varepsilon} \cos (kx + \phi) \right) \frac{E - \varepsilon}{\sqrt{(E - \varepsilon)^2 - \Delta^2}},$$

where ρ_0 is the spatially average DOS at the Fermi energy, ε is the center energy of the CDW gap, Δ is the CDW gap size, ϕ is the phase of CDW in real space, $k = 2\pi/\lambda$ is the wave vector, and λ is the wavelength of the CDW. Here, we assumed that 1D CDW dispersion is

$$E_k = \text{sgn}(\epsilon_k)\sqrt{\epsilon_k^2 + \Delta^2},$$

and the normal-state dispersion is linearized around the Fermi energy:

$$\epsilon_k = \hbar v_F (k - k_F).$$

To reproduce the experimentally obtained CDWs, we added local DOSs of multiple CDWs with the form of a 1D CDW model, $\rho_i(E, x)$, at different center energy (ε_i) and phase (ϕ_i) without considering the weight:

$$\rho(E, x) = \sum_i \rho_i(E, x).$$

We used the experimentally obtained gap energies of $\mathbf{q}_1$ and $\mathbf{q}_2$ CDW, which are marked in Figs. 4(c) and 4(f), respectively. The parameters used in the simulation are summarized in Table I. As shown in Fig. 9, the simulation results captured the experimental observation of energy-dependent phase shift and DOS suppressions. This toy model with a multiple CDW gap verifies the multiband nature of CDWs formed on a surface of NbTe$_2$.

[1] R. M. Martin, L. Reining, and D. M. Ceperley, *Interacting Electrons* (Cambridge University Press, Cambridge, 2016).

[2] R. E. Peierls, *Quantum Theory of Solids* (Oxford University Press, Oxford, 1955).

[3] K. Rossnagel, J. Phys.: Condens. Matter **23**, 213001 (2011).

[4] A. H. Castro Neto, Phys. Rev. Lett. **86**, 4382 (2001).

[5] M. Liu, J. Leveillee, S. Lu, J. Yu, H. Kim, C. Tian, Y. Shi, K. Lai, C. Zhang, F. Giustino, and C.-K. Shih, Sci. Adv. **7**, eabi6339 (2021).

[6] M. M. Ugeda, A. J. Bradley, Y. Zhang, S. Onishi, Y. Chen, W. Ruan, C. Ojeda-Aristizabal, H. Ryu, M. T. Edmonds, H.-Z. Tsai *et al.*, Nat. Phys. **12**, 92 (2016).

[7] G. Grüner, Rev. Mod. Phys. **60**, 1129 (1988).

[8] X. Zhu, Y. Cao, J. Zhang, E. W. Plummer, and J. Guo, Proc. Natl. Acad. Sci. USA **112**, 2367 (2015).

[9] M. D. Johannes and I. I. Mazin, Phys. Rev. B **77**, 165135 (2008).

[10] M. Spera, A. Scarfato, A. Pásztor, E. Giannini, D. R. Bowler, and C. Renner, Phys. Rev. Lett. **125**, 267603 (2020).

[11] J. Hwang, K. Kim, C. Zhang, T. Zhu, C. Herbig, S. Kim, B. Kim, Y. Zhong, M. Salah, M. M. El-Desoky, C. Hwang, Z.-X. Shen, M. F. Crommie, and S.-K. Mo, Nat. Commun. **13**, 906 (2022).

[12] Á. Pásztor, A. Scarfato, M. Spera, F. Flicker, C. Barreteau, E. Giannini, J. van Wezel, and C. Renner, Nat. Commun. **12**, 6037 (2021).

[13] C. Battaglia, H. Cercellier, F. Clerc, L. Despont, M. G. Garnier, C. Koitzsch, P. Aebi, H. Berger, L. Forró, and C. Ambrosch-Draxl, Phys. Rev. B **72**, 195114 (2005).

[14] J. van Landuyt, G. van Tendeloo, and S. Amelinckx, Phys. Status Solidi A **26**, 585 (1974).

[15] D. Cukjati, A. Prodan, N. Jug, H. J. P. Van Midden, S. W. Hla, H. Böhm, F. W. Boswell, and J. C. Bennett, Phys. Status Solidi **193**, 246 (2002).

[16] H. Chen, Z. Li, X. Fan, L. Guo, and X. Chen, Solid State Commun. **275**, 16 (2018).

[17] A. H. Barajas-Aguilar, J. C. Irwin, A. M. Garay-Tapia, T. Schwarz, F. Paraguay Delgado, P. M. Brodersen, R. Prinja, N. Kherani, and S. J. Jiménez Sandoval, Sci. Rep. **8**, 16984 (2018).

[18] H. Wang, K. Chai, L. Wei, Z.-A. Li, C. Zhu, D. Zheng, Z. Li, J. Li, H. Tian, H. Yang, and J. Li, Europhys. Lett. **130**, 47001 (2020).

[19] F. Tang, H. C. Po, A. Vishwanath, and X. Wan, Nature (London) **566**, 486 (2019).

[20] X. Zhang, T. Luo, X. Hu, J. Guo, G. Lin, Y. Li, Y. Liu, X. Li, J. Ge, Y. Xing, Z. Zhu, P. Gao, L. Sun, and J. Wang, Chin. Phys. Lett. **36**, 057402 (2019).

[21] J. A. Wilson, Phys. Rev. B **17**, 3880 (1978).

[22] H. Feng, Z. Xu, J. Zhuang, L. Wang, Y. Liu, X. Xu, L. Song, W. Hao, and Y. Du, Adv. Funct. Mater. **29**, 1900367 (2019).

[23] H. Bengel, H.-J. Cantow, S. N. Magonov, and M.-H. Whongbo, Adv. Mater. **7**, 483 (1995).

[24] S. Nagata, T. Abe, S. Ebisu, Y. Ishihara, and K. Tsutsumi, J. Phys. Chem. Solids **54**, 895 (1993).

[25] I. E. Baggari, B. H. Savitzky, A. S. Admasu, J. Kim, S. W. Cheong, R. Hovden, and L. F. Kourkoutis, Proc. Natl. Acad. Sci. USA **115**, 1445 (2018).

[26] A. Pásztor, A. Scarfato, M. Spera, C. Barreteau, E. Giannini, and C. Renner, Phys. Rev. Research **1**, 033114 (2019).

[27] D. Stoltz, M. Bielmann, M. Bovet, L. Schlapbach, and H. Berger, Phys. Rev. B **76**, 073410 (2007).

[28] W. L. McMillan, Phys. Rev. B **12**, 1187 (1975).

[29] J. Dai, E. Calleja, J. Alldredge, X. Zhu, L. Li, W. Lu, Y. Sun, T. Wolf, H. Berger, and K. McElroy, Phys. Rev. B **89**, 165140 (2014).